



Supplementary Materials for

A highly active and stable $\text{IrO}_x/\text{SrIrO}_3$ catalyst for the oxygen evolution reaction

Linsey C. Seitz, Colin F. Dickens, Kazunori Nishio, Yasuyuki Hikita, Joseph Montoya, Andrew Doyle, Charlotte Kirk, Aleksandra Vojvodic, Harold Y. Hwang, Jens K. Nørskov, Thomas F. Jaramillo*

*Corresponding author. Email: jaramillo@stanford.edu

Published 2 September 2016, *Science* **353**, 1011 (2016)
DOI: 10.1126/science.aaf5050

This PDF file includes:

Materials and Methods
Figs. S1 to S8
Tables S1 to S2
Full Reference List

Title: A Highly Active and Stable IrO_x/SrIrO₃ Catalyst for the Oxygen Evolution Reaction

Authors: Linsey C. Seitz¹, Colin F. Dickens^{1,2}, Kazunori Nishio^{3,4}, Yasuyuki Hikita³, Joseph Montoya², Andrew Doyle², Charlotte Kirk², Aleksandra Vojvodic², Harold Y. Hwang^{3,4}, Jens K. Nørskov^{1,2}, Thomas F. Jaramillo^{1,2*}

Affiliations:

¹SUNCAT Center for Interface Science and Catalysis, Department of Chemical Engineering, Stanford University, Shriram Center, 443 Via Ortega, Stanford, California, 94305, USA.

²SUNCAT Center for Interface Science and Catalysis, SLAC National Accelerator Laboratory 2575 Sand Hill Road, Menlo Park, California, 94025, USA

³Stanford Institute for Materials and Energy Sciences, SLAC National Accelerator Laboratory 2575 Sand Hill Road, Menlo Park, California, 94025, USA

⁴Geballe Laboratory for Advanced Materials, Department of Applied Physics, Stanford University, 476 Lomita Mall, Stanford, California, 94305, USA.

*Correspondence to: jaramillo@stanford.edu

Supplementary Material:

Materials and Methods

Sample Preparation

Pulsed laser deposition (PLD) was used to fabricate the SrIrO₃ films onto insulating SrTiO₃ (100) substrates. A pulsed excimer laser (KrF, wavelength 248 nm) was imaged onto a SrIrO₃ polycrystalline target at the laser fluence of 3.75 J/cm² and laser repetition rate of 3 Hz. The substrate was maintained at 650 °C in partial oxygen pressure of 300 mTorr during growth. The film thickness was controlled by setting the laser pulse counts.

Identification of Crystal Structure

Material crystallinity was confirmed using XRD, before and after electrochemical testing; sample size of as prepared samples was 5 x 5 mm², while the measured sample size of samples after 30 minutes electrochemical testing was 2.5 x 5 mm². A monochromated Cu K_{α1} (λ = 1.54056 Å) tube was used as the X-ray source (D8 Discover, Bruker AXS) and 2theta/omega scans were taken after aligning the samples with respect to the SrTiO₃ 200 diffraction peak. All spectral intensities are plotted in log scale with respect to 2theta.

Investigation of Film Morphology

Atomic force microscopy (AFM) was used to determine the morphology of the PLD films, both as deposited and after electrochemical testing. Bruker Dimension 3000 was used in non-contact mode for all topography measurements.

Identification of Surface Composition and Chemical State

X-ray photoelectron spectroscopy (XPS) was performed using a Phi VersaProbe spectrometer with an Al K α source, and binding energies were calibrated to the adventitious C 1s peak at 284.8 eV. Film surface and chemical compositions were determined using MultiPak (Physical Electronics, Inc.) and CasaXPS (Casa Software Ltd) fitting software. Peak areas were calculated for Ir4f in the range of 60-70 eV and normalized to be equal. Peak areas were then calculated for Sr3d and Sr3p in the ranges of 130-138 eV and 283-291 eV, respectively, and normalized using the respective factors from Ir normalization for each sample. The relative quantities of Sr and Ir in the sputtering depth profile measurements were determined using the Sr3d and Ir4f peak areas normalized by sensitivity factors from the fitting software.

Electrochemical Testing

Copper wires were attached to the perimeter of the SrIrO₃ films using ultrasonic solder and samples were epoxied such that only SrIrO₃ film was exposed. Catalytic activity was assessed using cyclic voltammetry (CV, BioLogic, VSP) with a sweep rate of 10 mV/s in a 3 electrode electrochemical set-up with a coiled platinum wire counter electrode and Hg/Hg₂SO₄ in saturated K₂SO₄ reference electrode (Hach). All experiments were performed in 0.5 M sulfuric acid (H₂SO₄) electrolyte prepared with MilliQ water at room temperature while purging with oxygen. All data were post corrected for 100% of the solution series resistance measured by impedance spectroscopy (PEIS measured at open circuit from 500 kHz to 1 Hz with an amplitude of 10 mV) and shifted to a reversible hydrogen electrode (RHE) scale by calibrating the Hg/Hg₂SO₄ reference electrode using coiled platinum wire working and counter electrodes under a H₂ gas purge. For extended testing, a procedure similar to previously reported benchmarking was used (1). The working electrode was held at a fixed current of 10 mA/cm²_{geo} for 2, 4 or 8 hours, followed by electrochemical impedance measurement (PEIS), 5 CV scans (10 mV/s, voltage range adjusted to reach at least 10 mA/cm²_{geo}).

Quantification of Sr and Ir in Electrolyte after Testing (ICP-OES)

Fresh SrIrO₃ films were tested electrochemically with CVs using the same procedure as described above for approximately 30 minutes in 15 mL 0.5 M H₂SO₄ electrolyte. The electrolyte was then diluted to 0.1 M, passed through a 0.45 μ m filter and analyzed using inductively coupled plasma optical emission spectroscopy (ICP-OES) on a Thermo Scientific ICAP 6300 Duo View Spectrometer to determine the concentration of Sr. Blank and standard solutions with Sr at 25 μ g/L and 50 μ g/L were prepared using a 1000 mg/L Sr ICP standard (Ricca Chemical) for instrument calibration.

DFT Calculations

All DFT calculations were performed using the Atomic Simulation Environment (24) in combination with Quantum ESPRESSO (25) with the revised Perdew-Burke-Ernzerhof (RPBE) exchange-correlation functional (26). Cutoff energies of 600 and 6000 eV were used for wavefunctions and electron density, respectively. Core electrons were replaced by ultrasoft pseudopotentials.

Rutile and anatase IrO₂ bulk structures were optimized over their lattice constants a and c and an internal coordinate u , resulting in $a = 4.584, 3.956$ Å; $c = 3.207, 9.900$ Å; and $u = 0.308, 0.207$ for rutile and anatase, respectively. SrIrO₃ bulk structure was assumed to be cubic for simplicity (allowing unit cell to become tetragonal/orthorhombic had little effect on adsorption energies)

and was found by optimizing over the lattice constant and allowing all atoms of a $2 \times 2 \times 2$ supercell (4, 4, 4 Monkhorst-Pack k-point sampling) to relax at each iteration, resulting in $a = 4.024 \text{ \AA}$.

Surface calculations were performed with a $2 \times 2 \times 4$ supercell for anatase IrO_2 (001), SrIrO_3 (001)- BO_2 , and all Sr-deficient SrIrO_3 structures; a $1 \times 3 \times 4$ supercell for rutile IrO_2 (110); and a $2 \times 3 \times 4$ supercell for rutile IrO_2 (100). All surface calculations used a (4, 4, 1) Monkhorst-Pack k-point sampling. Pure IrO_2 surface calculations kept 2 layers fixed; SrIrO_3 (001), $\text{IrO}_3/\text{SrIrO}_3$ (2 ML) structures kept 2 SrO layers and 1 IrO_2 layer fixed; and $\text{IrO}_3/\text{SrIrO}_3$ (3 ML), IrO_2 -sheets/ SrIrO_3 (2 ML), and IrO_2 -anatase/ SrIrO_3 (2 ML) kept 1 SrO layer and 1 IrO_2 layer fixed. For stability calculations, a common number of fixed layers was used for each surface.

Ab initio molecular dynamics were also performed within the Atomic Simulation Environment using Langevin dynamics with a temperature of 1000 °C, time-step of 5 femtoseconds, and friction parameter of 0.002 atomic units. A $1 \times 1 \times 4$ supercell of SrIrO_3 with 2ML anatase IrO_2 was used as the starting point. IrO_2 -sheets emerged after 30 picoseconds of simulation, at which point the system was relaxed to the structure shown in Fig. 3E. Continuing molecular dynamics beyond 30 picoseconds resulted in desorption of the IrO_2 overlayer.

Tafel Plot

Figure S1A shows example CVs of $\text{IrO}_x/\text{SrIrO}_3$ taken periodically during electrochemical stability testing. Figure S1B shows a Tafel plot of the intrinsic, or specific, activities for the best reported catalysts in both acidic and alkaline electrolyte as replicated from literature. Specific activities were either taken directly from literature or calculated using reported catalyst surface area or roughness factor. If no roughness factor was specified for thin, nearly flat films, a roughness factor of one was approximated. In this work, $\text{IrO}_x/\text{SrIrO}_3$ was not tested in alkaline electrolyte; for comparison, Figure S1B includes measurements from a similar catalyst system studied in alkaline media, SrIrO_3 synthesized using molecular beam epitaxy.⁽¹¹⁾

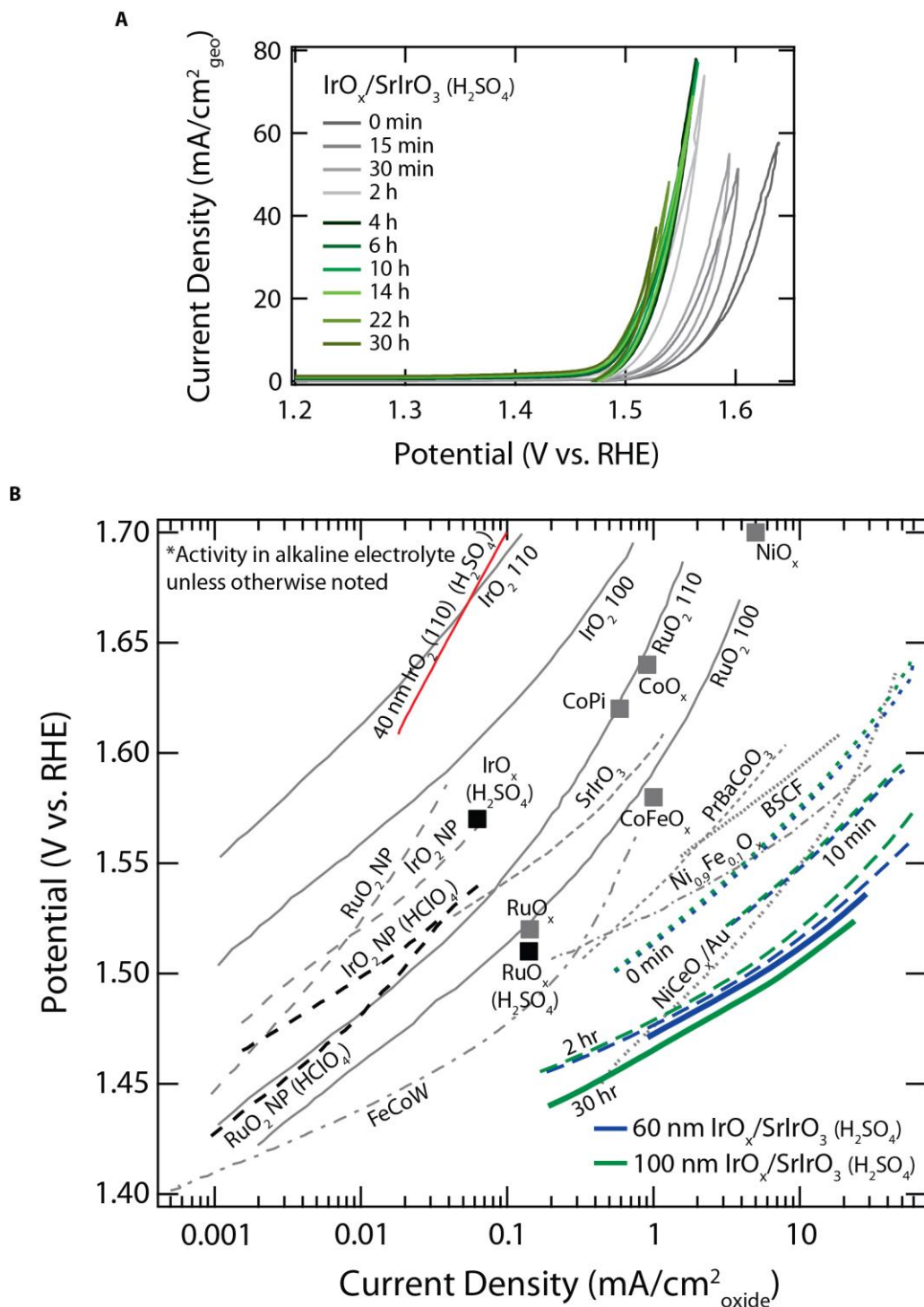


Fig. S1. Electrochemical Activity. (A) Cyclic voltammograms showing geometric current density of a 100 nm $\text{IrO}_x/\text{SrIrO}_3$ film at several times during 30 hours of electrochemical stability testing. CVs representing activity for 4 hours through 14 hours are overlapping. (B) Tafel plot comparing specific activity of $\text{IrO}_x/\text{SrIrO}_3$ to OER catalysts in acidic and alkaline electrolyte. Colored lines are from this work. Green lines show 100 nm $\text{IrO}_x/\text{SrIrO}_3$ and blue lines show 60 nm $\text{IrO}_x/\text{SrIrO}_3$ specific activity at various points during electrochemical stability testing. The

red line shows specific activity for 40 nm rutile IrO₂ (110) film. Gray and black lines/markers are duplicated from literature for catalysts in alkaline and acidic conditions, respectively (1-3, 5, 11, 13, 27-29).

There are a number of published electrodes which have achieved high OER activities that are not included in Figure S1B; for example, there are several reports of high surface area electrodes using NiFeO_x catalysts tested in alkaline electrolyte which demonstrate high current densities at low overpotentials.(30-33) Similarly, IrO_x-based catalysts tested in acidic electrolyte often demonstrate high electrode activities when synthesized in high surface area nanoparticulate geometries or when using high mass loading.(13, 34) However, it is important to distinguish between electrode activity normalized to the geometric area of the electrode, and intrinsic or specific catalyst activity which is normalized to the actual catalyst surface area. Increasing catalyst loadings or improving catalyst geometries to expose large surface areas on small electrodes can lead to improved performance which are useful for many applications, but it remains an important fundamental pursuit to improve specific catalyst activity normalized to actual catalyst surface area. Most NiFeO_x-based and IrO_x-based catalysts have similar intrinsic activity when they are normalized to their actual catalyst surface area. However, by simultaneously improving intrinsic catalyst activity and then applying engineering schemes to increase exposed surface area or active sites, one can achieve even better electrode performances. For the sake of clarity, Figure S1B shows representative activities for catalyst systems with the highest intrinsic activities available in literature.

Theoretical Evaluation of Activity

The calculation of electrochemical barriers in aqueous environments using DFT is still quite difficult compared to thermal, gas phase systems (35). However, due to the fact that the energetics of transition states and intermediates scale with one another, thermodynamic descriptors can be useful in predicting and explaining trends in catalytic activity. One such method for electrochemical reactions that has proven successful is the calculation of theoretical overpotential, which is the overpotential required to make all elementary steps of a mechanism exergonic (14). The free energy change of any elementary step that involves the production of a proton-electron pair will decrease linearly with applied potential versus the RHE:

$$\Delta G = \Delta G^\circ - eU_{\text{RHE}} \quad (1)$$

such that the potential at which the step becomes downhill (the limiting potential, U_L) may be calculated as

$$U_L = \Delta G^\circ / e \quad (2)$$

and thus the theoretical overpotential is written

$$\eta = \max_i (\Delta G_i^\circ) / e - E^\circ \quad (3)$$

where E° is the equilibrium potential of the reaction (1.23 V in the case of OER) and e is the fundamental unit of charge.

We consider four elementary steps for the OER, with each consisting of a single proton electron transfer:



where * represents a surface site. The free energy of each adsorbate is calculated at 0 V vs RHE by referencing to liquid water and hydrogen gas at standard conditions:

$$\Delta G_{OH} = E_{OH^*}^{DFT} - E_*^{DFT} - \mu_{\text{H}_2\text{O}(l)}^0 + \frac{1}{2} \mu_{\text{H}_2(g)}^0 - \hat{G}_{OH^*} \quad (8)$$

$$\Delta G_O = E_{O^*}^{DFT} - E_*^{DFT} - \mu_{\text{H}_2\text{O}(l)}^0 + \mu_{\text{H}_2(g)}^0 - \hat{G}_{O^*} \quad (9)$$

$$\Delta G_{OOH} = E_{OOH^*}^{DFT} - E_*^{DFT} - 2\mu_{\text{H}_2\text{O}(l)}^0 + \frac{3}{2} \mu_{\text{H}_2(g)}^0 - \hat{G}_{OOH^*} \quad (10)$$

where \hat{G}_i includes contributions from vibrational energy (zero point energy and internal energy) and entropy of the adsorbate at 300 K. This correction was calculated using the harmonic approximation for every adsorbate and surface studied, with typical values of 0.35, 0.05, and 0.40 for OH*, O*, and OOH*, respectively. Using hydrogen gas as a reference is acceptable at 0 V vs RHE because of the RHE definition:

$$\mu_{\text{H}^+/\text{e}^-}^0 = \frac{1}{2} \mu_{\text{H}_2(g)}^0 \quad (11)$$

To avoid calculating the energy of liquid water in DFT, we exploit gas-liquid equilibrium of H₂O:

$$\mu_{\text{H}_2\text{O}(l)}^0 = \mu_{\text{H}_2\text{O}(g)} \Big|_{p=0.035 \text{ bar}} @ T=300\text{K} \quad (12)$$

The standard free energy change of each elementary step may then be calculated:

$$\Delta G_1^0 = \Delta G_{OH} \quad (13)$$

$$\Delta G_2^0 = \Delta G_O - \Delta G_{OH} \quad (14)$$

$$\Delta G_3^0 = \Delta G_{OOH} - \Delta G_O \quad (15)$$

$$\Delta G_4^0 = \Delta G_{\text{O}_{2(g)}}^0 - \Delta G_{OOH} \quad (16)$$

DFT is well-known to struggle at describing the O₂ molecule, so we instead substitute the experimental formation energy of H₂O when calculating the final step:

$$\begin{aligned} 2\text{H}_2 + \text{O}_2 &\rightarrow 2\text{H}_2\text{O} & \Delta G^0 &= -4.92 \text{ eV} \\ \Delta G_{\text{O}_{2(g)}}^0 &= 4.92 \text{ eV} \end{aligned} \quad (17)$$

The energetics of each step were calculated for all surfaces and coverages considered, and the theoretical overpotential was calculated using Equation (3). Adsorption energies were only accepted if the placement of each adsorbate did not appreciably distort the surface. In the event

that the placement of a single adsorbate distorted the surrounding atoms differently than when other adsorbates were placed, each adsorbate was placed on the newly distorted surface. For the IrO_3 overlayer structures in particular, we observed distortion of the top two layers as the various OER adsorbates were added to the surface, leading to asymmetry in the four on-top Ir sites. We calculated $\Delta G_O - \Delta G_{OH}$ to range from 0.8 to 1.8 eV between the sites at various levels of distortion, suggesting an IrO_3 film may possess sites with a variety of bonding environments and that some fraction of them are highly active for the OER. Encompassing all of these active sites with a single structure would require the use of a larger supercell.

Choice of Surface Coverages

Adsorbate-adsorbate interactions play a role in the catalytic activity of a surface by influencing the energetics of surface-bound intermediates (36). Recent OER studies have taken this into account by calculating binding energies of OH^* , O^* , OOH^* at a thermodynamically self-consistent coverage by first creating a surface Pourbaix diagram and identifying the most stable coverage at the limiting OER potential for the surface in question (37, 38). Ultimately, the surface coverage is dictated by kinetics for potentials greater than 1.23 V vs. RHE (where oxygen is not able to build up a sufficient backpressure to maintain equilibrium in a typical experimental setup), and here we present a simple way of understanding this kinetically-controlled coverage. This methodology will be presented in greater detail in a future study, but because it has influenced our selection of relevant coverages in the present work, a brief summary is provided here.

For potentials greater than the limiting potential, where all elementary steps are downhill and backwards reaction rates are negligible, the reaction rate r_i of each step may be written

$$r_i \approx \theta_i k_i \quad (18)$$

where θ_i is the coverage of reactant corresponding to reaction i and k_i is the forward rate constant of reaction i (it is assumed that $\text{O}_{2(g)}$ is in its standard state). The accumulation of coverage of each surface-bound intermediate can then be written as

$$\frac{\partial \theta_{\text{OH}}}{\partial t} = \theta_* k_1 - \theta_{\text{OH}} k_2 \quad (19)$$

$$\frac{\partial \theta_{\text{O}}}{\partial t} = \theta_{\text{OH}} k_2 - \theta_{\text{O}} k_3 \quad (20)$$

$$\frac{\partial \theta_{\text{OOH}}}{\partial t} = \theta_{\text{O}} k_3 - \theta_{\text{OOH}} k_4 \quad (21)$$

$$\frac{\partial \theta_*}{\partial t} = \theta_{\text{OOH}} k_4 - \theta_* k_1 \quad (22)$$

and thus at steady-state:

$$\theta_* k_1 = \theta_{\text{OH}} k_2 = \theta_{\text{O}} k_3 = \theta_{\text{OOH}} k_4 \quad (23)$$

such that the step with the largest barrier (smallest k) will have the highest coverage. Assuming that the thermodynamic height of each step correlates with the barrier height (i.e. all barriers scale similarly with potential and all steps have similar barriers at a given thermodynamic driving force), surfaces that fall on the left, right, top, or bottom legs of the theoretical

overpotential volcano shown in Figure 2A will be covered by O*, OH*, *, or OOH*, respectively, above the limiting potential. In this framework, a calculation is self-consistent if it is performed at a particular coverage and is found to lie on the leg of the volcano that corresponds to that coverage. Figure S2 shows calculations for all surfaces considered in this study at various coverages. To account for the assumptions made about the barriers in this analysis and for the intrinsic error of DFT, we consider a calculation self-consistent if the step height corresponding to the coverage at which the calculation was performed is the largest step height or within 0.1 eV of the largest step height. Mixed (binary) coverages were also considered and accepted as self-consistent if the step heights corresponding to each constituent of the coverage at which the calculation was performed are the largest step heights and are within 0.1 eV of each other. In the event that there are multiple self-consistent coverages, we choose the most active coverage since it should dominate the observed rate. The mixed O/OH coverages (triangles) nearest to $\Delta G_O - \Delta G_{OH} = 1.45$ eV for anatase IrO₂ (001) and SrIrO₃ with 2ML anatase IrO₂ correspond to 2 O coadsorbates and 1 OH coadsorbate, while the other mixed O/OH coverages for these surfaces correspond to 2OH coadsorbates and 1 O coadsorbate.

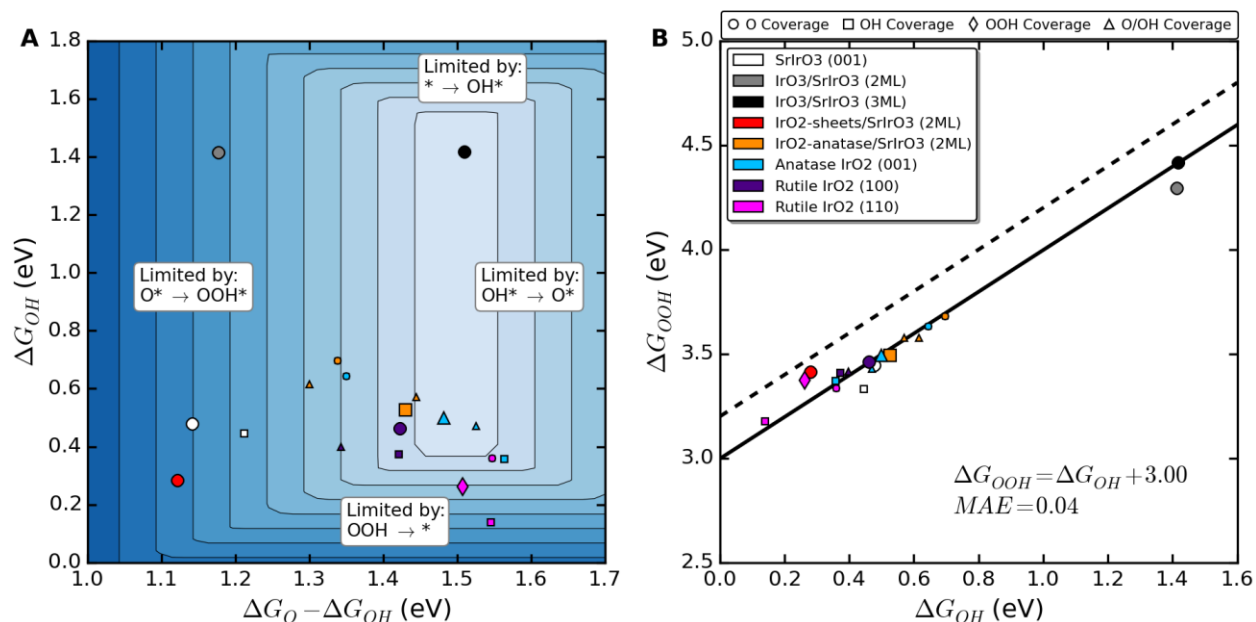


Fig. S2. OER theoretical overpotential volcano and OH/OOH scaling relation for all surfaces and coverages considered. (A) Theoretical overpotential volcano where each leg is labeled by the step limiting OER performance. Larger symbols represent points that are featured in Figure 2 of the main text. (B) Scaling relation between ΔG_{OH} and ΔG_{OOH} . The dotted line represents the “universal” scaling line that has been found to describe a wide variety of metal-oxide materials, $\Delta G_{OOH} = \Delta G_{OH} + 3.2$ eV (14).

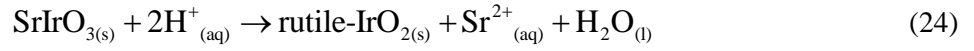
OH/OOH Scaling Relation

A scaling relationship between OH and OOH is shown in Figure S2B. In previous work, Man *et al.* (14) suggest that the large OER overpotentials observed for many oxides can be explained by linear correlations between OH and OOH adsorption energies, which scale with an almost

materials-independent difference of 3.2 +/- 0.2 eV. The structures considered in this study are concentrated at the lower bound of this range, with a scaling relationship intercept of 3.0 eV. This suggests that the most active surfaces considered here nearly achieve the lowest possible OER overpotential without breaking the correlation between adsorbed OH and OOH.

Theoretical Evaluation of Stability

The dissolution of SrIrO₃ to form Sr²⁺ and rutile IrO₂ can be written as



$$\Delta G = \mu_{\text{IrO}_2}^0 + \mu_{\text{Sr}^{2+}}^0 + \mu_{\text{H}_2\text{O}}^0 - \mu_{\text{SrIrO}_3}^0 - 2\mu_{\text{H}^+}^0 + k_B T \ln \frac{[\text{Sr}^{2+}]}{[\text{H}^+]^2} \quad (25)$$

Utilizing the electrochemical series to eliminate Sr²⁺ (39) and approximating the chemical potential of solids as their total energy from DFT (36):

$$\mu_{\text{Sr}^{2+}}^0 = \mu_{\text{Sr}}^0 - 2\mu_{\text{e}^-}^0 + 2eE_{\text{Sr/Sr}^{2+}}^0 \quad (26)$$

$$\mu_{\text{IrO}_2}^0 + \mu_{\text{Sr}}^0 - \mu_{\text{SrIrO}_3}^0 \approx E_{\text{IrO}_2}^{\text{DFT}} + E_{\text{Sr}}^{\text{DFT}} - E_{\text{SrIrO}_3}^{\text{DFT}} \quad (27)$$

$$\Delta G = E_{\text{IrO}_2}^{\text{DFT}} + E_{\text{Sr}}^{\text{DFT}} - E_{\text{SrIrO}_3}^{\text{DFT}} - \mu_{\text{H}_2}^0 + \mu_{\text{H}_2\text{O}}^0 + 2E_{\text{Sr/Sr}^{2+}}^0 + k_B T \ln \frac{[\text{Sr}^{2+}]}{[\text{H}^+]^2} \quad (28)$$

$$\Delta G_{T=300\text{K}} = \left(-3.25 + 0.118\text{pH} + 0.059 \log \frac{[\text{Sr}^{2+}]}{10^{-6} \text{ M}} \right) \text{ eV/Sr}$$

Similarly, the free energy of dissolving two monolayers of Sr from a stoichiometric SrIrO₃ (001) surface to form anatase-IrO₂/SrIrO₃ (2ML) can be written and calculated as



$$\Delta G = \left(E_{\text{IrO}_2/\text{SrIrO}_3}^{\text{DFT}} - E_{\text{SrIrO}_3}^{\text{DFT}} \right) / 8 + E_{\text{Sr}}^{\text{DFT}} - \mu_{\text{H}_2}^0 + \mu_{\text{H}_2\text{O}}^0 - \hat{G}_{\text{O}^*} + 2E_{\text{Sr/Sr}^{2+}}^0 + k_B T \ln \frac{[\text{Sr}^{2+}]}{[\text{H}^+]^2} \quad (30)$$

$$\Delta G_{T=300\text{K}} = \left(-2.18 + 0.118\text{pH} + 0.059 \log \frac{[\text{Sr}^{2+}]}{10^{-6} \text{ M}} \right) \text{ eV/Sr} \quad (31)$$

In this case, O is treated as a surface adsorbate, and its free energy correction is included. The ΔE between the surface calculations is divided by 8 to account for two monolayer depletion in a 2 × 2 unit cell.

Finally, the free energy change associated with oxidizing two monolayers of IrO₂ sheets to form IrO₃ does not involve Sr leaching and is simply calculated as the adsorption of eight O atoms (2 monolayers) in the 2 × 2 unit cell according to equation (9):

$$\Delta G_{T=300\text{K}} = (2.43 - 2eU_{\text{RHE}}) \text{ eV/O} \quad (32)$$

Additional AFM Maps and Line Scans

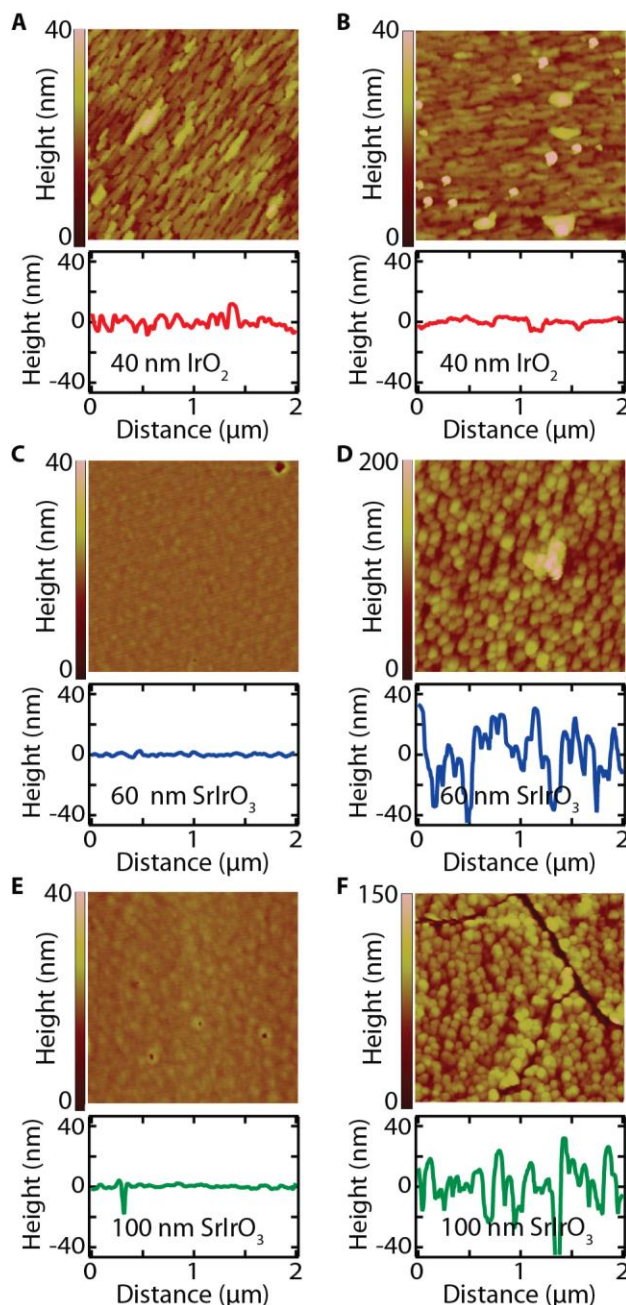


Fig. S3. AFM maps and line scans. AFM of IrO₂ and SrIrO₃ PLD films before (A, C, E) and after (B, D, F) 30 hours of electrochemical testing.

The notable result from AFM measurements is that all samples, tested or untested, are remarkably flat as is shown in Figure S3. The table in the main text Figure 3B also summarizes the roughness factor (RF) and RMS roughness of these samples. Before testing, all samples have an RF between 1.00 and 1.02 with RMS roughness less than 4 nm. After stability testing, the RF of all samples remained low, between 1.00 and 1.20, with RMS roughness less than 20 nm.

Additional XRD

X-ray diffractograms shown in Figure S4 for the SrIrO_3 films on SrTiO_3 display all the characteristic peaks for the expected pseudo-cubic structure. The SrIrO_3 peaks are located at smaller 2 theta values compared to the corresponding peaks for SrTiO_3 due to its slightly larger lattice. There is some decrease in SrIrO_3 peak intensity after 30 hours of electrochemical testing, as can be seen in the enlarged 200 peak in Figure S4B. There are no additional peaks visible after electrochemical testing that would indicate potential formation of new crystalline surface phases, but these few surface layers would likely be too thin to be detected with this technique.

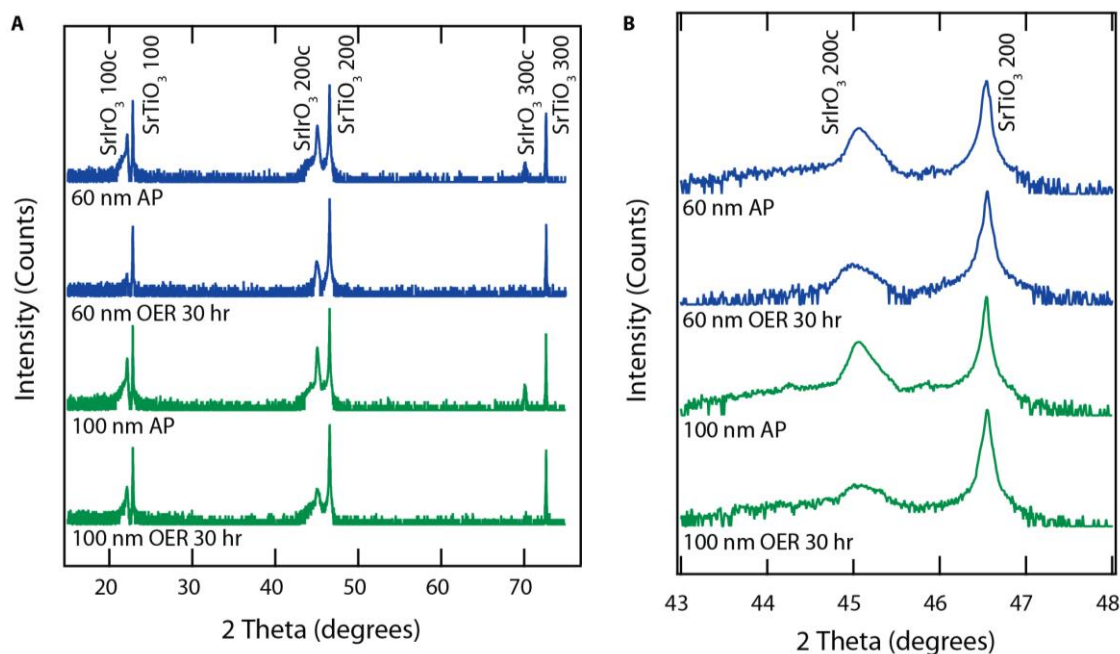


Fig. S4. XRD for SrIrO_3 PLD films before (AP) and after 30 hours of electrochemical testing (OER 30 hr) showing large range (A) and zoom in (B) on the SrIrO_3 and SrTiO_3 200 peaks.

X-ray diffractograms shown in Figure S5 for the IrO_2 films on TiO_2 display all the characteristic peaks for the rutile structure. There is no detectable change in material crystallinity after 30 hours of electrochemical testing.

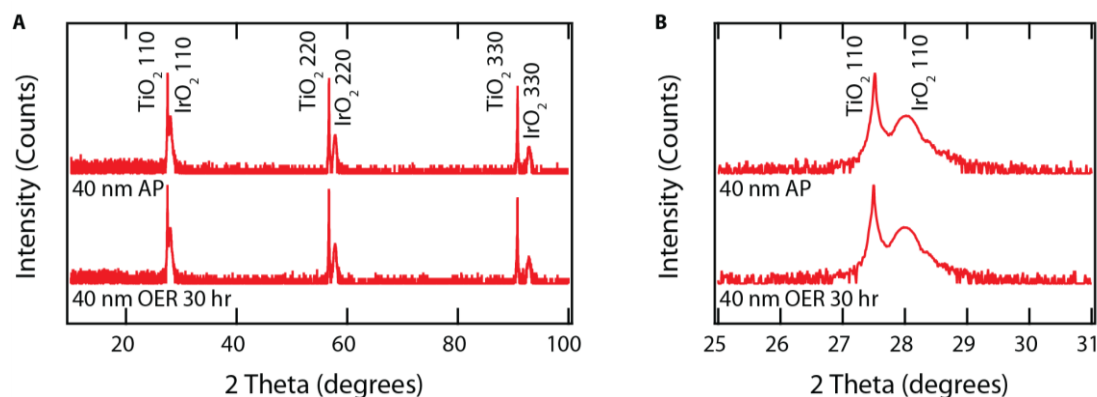


Fig. S5. XRD for 40 nm IrO₂ PLD film before and after 30 hours of electrochemical testing showing large range (A) and zoom in (B) on the IrO₂ and TiO₂ 110 peaks.

Additional XPS analysis

The surface composition and chemical state of the IrO_x/SrIrO₃ catalysts were assessed using X-ray photoelectron spectroscopy (XPS). XPS spectra of Ir4f and Sr3d probing the top 2-3 nm of material (about 10 monolayers) are shown in Figure S6 for both thicknesses of SrIrO₃ samples before (as prepared) and after 30 minutes of electrochemical OER testing. The peak areas are normalized to the Ir content, so they can be used as an indicator of relative film composition. The most obvious change in the spectra is that the Sr peaks have significantly decreased area after electrochemical testing, suggesting that Sr is leached from the surface which likely leads to rearrangement of the surface structure and is consistent with XRD and AFM results. Using sensitivity factors for the respective peaks, we determine that the as prepared films (before testing) have Sr-rich surfaces (2:1 Sr:Ir ratio), even though we would expect a 1:1 Sr:Ir ratio. This high Sr:Ir ratio may likely be caused by the growth kinetics. Given the low oxygen affinity of Ir, a relatively highly oxidizing condition is required for the growth. However, this simultaneously induces the formation of a gaseous species IrO₃ which can cause the SrIrO₃ surface to be Ir-deficient. Ruddlesen-Popper phases with formula Sr_{n+1}Ir_nO_{3n+1} (e.g. Sr₂IrO₄, Sr₃Ir₂O₇) are known to be stable and likely form in the top few surface layers with decreased Ir content (12, 40-42). After electrochemical testing, the surface Sr:Ir ratio is about 1:2, again indicating loss of Sr relative to the Ir. Using these normalized peak areas and the universal curve, we estimate that approximately the surface 7 monolayers have lost 100% of the Sr, (if we estimate that Sr first leaches completely from the surface-most monolayer and then proceeds to leach from subsequent monolayers) leaving only IrO₂ layers behind. However, this is a simplified estimation and it is likely that there is actually greater Sr loss in the topmost layers with gradually increasing Sr content towards the bulk concentration in subsurface layers as is shown in the depth profile sputtering results in the main text Figure 3E. Acid-etching and water-leaching of SrO from the surface of SrTiO₃ films is well known and has been used extensively to achieve TiO₂-terminated surfaces (43-47). Sr leaching has also been reported in other materials such as the highly active OER catalyst Ba_{0.5}Sr_{0.5}Co_{0.8}Fe_{0.2}O_{3-δ} (BSCF) which loses Sr and undergoes surface structural rearrangement during electrochemical cycling in basic electrolyte (48, 49).

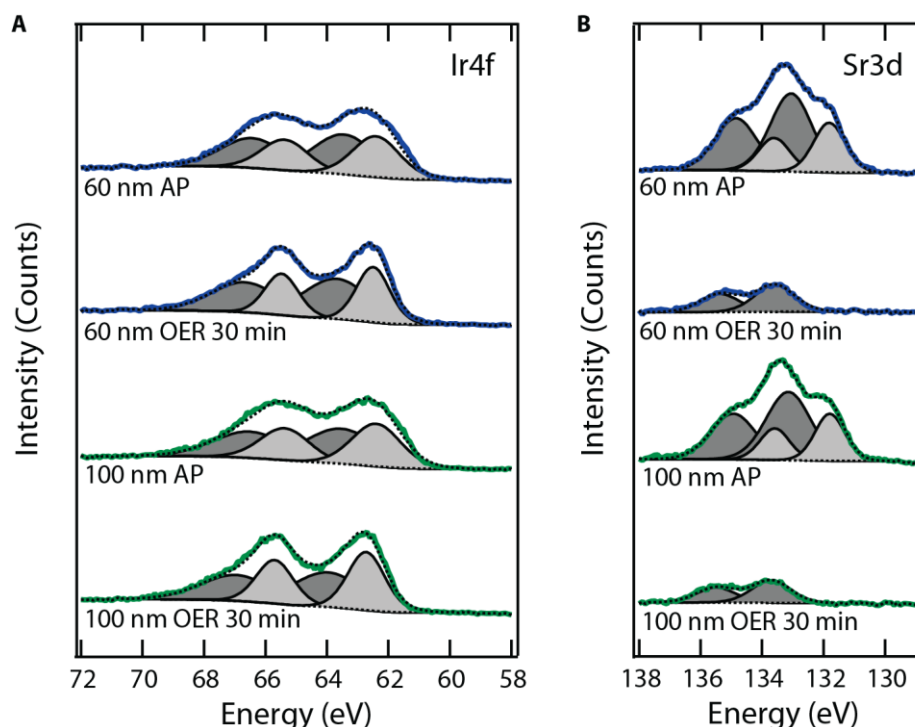


Fig. S6. XPS of the Ir4f (**A**) and Sr3d (**B**) for 60 nm and 100 nm IrO_x/SrIrO₃ films before and after 30 minutes of testing. Colored lines are the data, dotted lines indicate the baseline and fit sum of the doublets, shown in gray.

XPS peaks were also fit for the Sr3d and Ir4f edges (Figure S6) to determine chemical state contributions for each sample before and after electrochemical testing. The Ir4f peaks can be fit with two doublets for all samples, before and after electrochemical testing, with each doublet having a splitting of 2.98 eV and a relative area ratio of 4:3. In Figure S6A, the first doublet, shown in light gray, has the Ir4f 7/2 peak at approximately 62.3 eV and 62.6 eV for the samples as prepared and after electrochemical testing, respectively (Table S2). These peak positions are well within the expected range for IrO₂ (61.1 – 62.9 eV) but may also include a SrIrO₃ phase (61.8 eV), for which there are few literature references (40, 50). There is a nearly indistinguishable shift for SrIrO₃ vs. IrO₂, similar to the small reported shifts for SrO vs. SrTiO₃. It is interesting to note that the FWHM of the peaks becomes significantly narrower for this doublet after electrochemical testing. One potential explanation for this change is that there may be disorder in the as-prepared SrIrO₃ films due to Sr-excess cation stoichiometry which, after Sr leaching during electrochemistry, transitions to primarily an IrO₂ phase at the film surface. The second doublet, shown in darker gray, has an Ir4f 7/2 peak at approximately 63.4 eV and 63.8 eV for the samples as prepared and after electrochemical testing, respectively. This suggests the presence of an Ir phase in the presence of even more electronegative elements. The 1.1 eV shift between these two doublets is much larger than would be expected for other iridium oxide components and stabilization of Ir(V) or Ir(VI) oxide phases in vacuum is highly unlikely. The presence of this second doublet is likely due to a screening effect that has been observed previously (21). Various iridium halides and organometallics have also been reported with binding energies in this range, but presence of these compounds is also highly unlikely.

Table S2. Approximate XPS peak positions and full width half maxes (FWHM) for samples before and after 30 minutes of OER testing.

XPS Peak	Position (eV), as prepared	FWHM (eV), as prepared	Position (eV), after OER testing	FWHM (eV), after OER testing
Sr3d 5/2 A	131.8	1.2	N/A	N/A
Sr3d 5/2 B	133.1	1.7	133.7	1.5
Ir4f 7/2 A	62.3	1.7	62.6	1.3
Ir4f 7/2 B	63.4	2.5	63.8	2.5

The Sr3d peaks can be fit with two doublets for the as prepared films, but only one doublet is used to fit the peaks for the films after electrochemical testing since the peak shapes are not identical before and after testing. The doublets each have a splitting of 1.79 eV and a relative area ratio of 3:2. In Figure S6B, the first doublet, shown in light gray (only present in the as-prepared films), has the Sr3d 5/2 peak at approximately 131.8 eV with a full width half maximum (FWHM) of 1.2 eV. The second doublet, shown in darker gray, has the Sr3d 5/2 peak at approximately 133.1 eV and 133.7 eV, for the samples as prepared and after electrochemical testing, respectively. The FWHM of these peaks only changes slightly with electrochemical testing from 1.7 eV to 1.5 eV. Peak positions and FWHM are summarized in Table S2. There are a number of Sr chemical states that are reported in this range, including strontium metal (Sr, 132.1-134.4 eV), strontium (II) oxide (SrO, 132.5-132.9 eV), strontium hydroxide (Sr(OH)₂, 133.0 eV), strontium titanate (SrTiO₃, 132.7-133.1 eV), and strontium carbonate (SrCO₃, 132.9-133.5 eV) (50, 51). SrO, Sr(OH)₂, and SrCO₃ are very difficult to distinguish based on their Sr binding energies and all are expected to be present in SrO and more complex Sr oxides since Sr strongly chemisorbs to both carbon dioxide and water (52). None of these reference materials are within range to match the light gray doublet peaks at 131.8 eV, which is shifted to lower energy even than that of Sr metal. The darker gray doublet peaks likely represent a mix of phases including SrO, Sr(OH)₂, and SrCO₃ and potentially also SrIrO₃, for which there is no known published reference. The binding energy for SrIrO₃ might be expected to be very close to that of SrO and SrTiO₃ since the structures and surrounding elements are comparable and there is very little shift observed between SrO and SrTiO₃, even despite the presence of Ti. For the as-prepared samples, there is also a C1s peak (not shown) that is shifted to higher energies (287.3 eV) which matches other reported SrCO₃ peaks. After electrochemical testing, it is likely that there is less contribution from SrCO₃ since this C1s peak is no longer present and there is significantly less Sr at the surface; we expect that Sr in the subsurface layers mainly interacts with O and Ir.

Calibration Curve for ICP-OES

Inductively coupled plasma optical emission spectroscopy (ICP-OES) measurements of electrolyte after 30 minutes of electrochemical testing were calibrated using a set of prepared standards and also compared to a calibration curve, shown in Figure S7, to ensure accuracy.

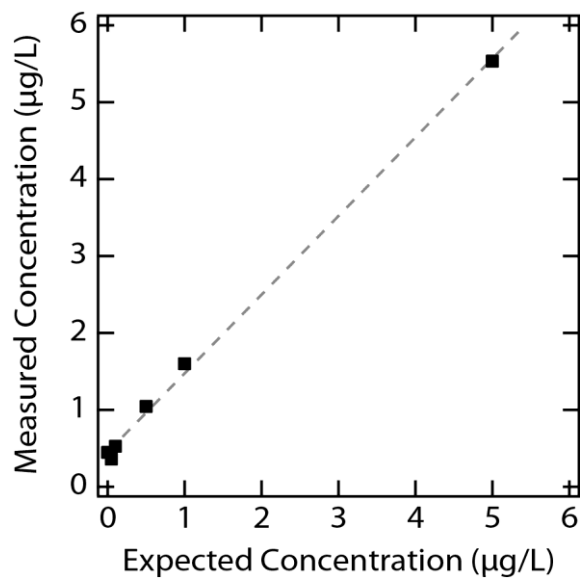


Fig. S7. Calibration curve for ICP-OES measurements. The data points are shown in black and the linear fit line shown in gray has a slope of 1.02 and an R^2 value of 0.998.

Investigation into role of SrIrO₃

To better understand the role of the SrIrO₃ within the IrO_x/SrIrO₃ system, very thin layers of IrO₂ were deposited onto bare SrIrO₃ using the same PLD methods employed for the other samples. These composite films were substantially more active than rutile IrO₂, providing further evidence of the importance of the underlying SrIrO₃ that can engender a more active phase of IrO_x. However, these composite films of IrO₂ deposited onto SrIrO₃ are not quite as active as the IrO_x/SrIrO₃ catalyst formed via Sr leaching from SrIrO₃ films, as is shown in Figure S8. This indicates that the surface IrO_x formed by means of the in situ leaching process of Sr from SrIrO₃ is different than that of purposely-deposited IrO_x, and more catalytically active.

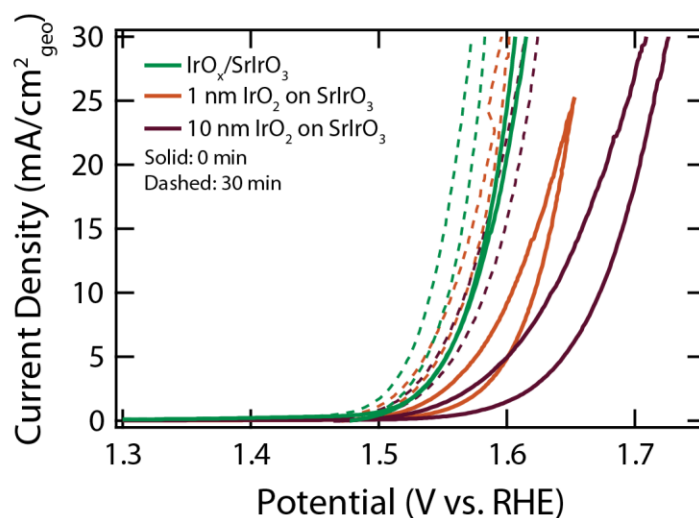


Fig. S8. Cyclic voltammograms showing geometric current density of a 100 nm IrO_x/SrIrO₃ film (with IrO_x surface layer formed via in situ Sr leaching from SrIrO₃) compared to two composite IrO₂/SrIrO₃ films (with IrO₂ deposited on top of SrIrO₃ using PLD) to illustrate superior activity of the catalyst formed via Sr-leaching from SrIrO₃. Both the leached film and the two composite films are more active than rutile IrO₂.

References and Notes

1. C. C. L. McCrory, S. Jung, I. M. Ferrer, S. M. Chatman, J. C. Peters, T. F. Jaramillo, Benchmarking hydrogen evolving reaction and oxygen evolving reaction electrocatalysts for solar water splitting devices. *JACS* **137**, 4347–4357 (2015). [doi:10.1021/ja510442p](https://doi.org/10.1021/ja510442p)
2. J. Suntivich, K. J. May, H. A. Gasteiger, J. B. Goodenough, Y. Shao-Horn, A perovskite oxide optimized for oxygen evolution catalysis from molecular orbital principles. *Science* **334**, 1383–1385 (2011). [Medline doi:10.1126/science.1212858](https://pubmed.ncbi.nlm.nih.gov/21521116/)
3. A. Grimaud, K. J. May, C. E. Carlton, Y. L. Lee, M. Risch, W. T. Hong, J. Zhou, Y. Shao-Horn, Double perovskites as a family of highly active catalysts for oxygen evolution in alkaline solution. *Nat. Commun.* **4**, 2439 (2013). [Medline doi:10.1038/ncomms3439](https://pubmed.ncbi.nlm.nih.gov/24391383/)
4. E. A. Paoli, F. Masini, R. Frydendal, D. Deiana, C. Schlaup, M. Malizia, T. W. Hansen, S. Horch, I. E. L. Stephens, I. Chorkendorff, Oxygen evolution on well-characterized mass-selected Ru and RuO₂ nanoparticles. *Chem. Sci.* **6**, 190–196 (2015). [doi:10.1039/C4SC02685C](https://doi.org/10.1039/C4SC02685C)
5. L. Trotochaud, J. K. Ranney, K. N. Williams, S. W. Boettcher, Solution-cast metal oxide thin film electrocatalysts for oxygen evolution. *JACS* **134**, 17253–17261 (2012). [doi:10.1021/ja307507a](https://doi.org/10.1021/ja307507a)
6. D. A. Corrigan, The catalysis of the oxygen evolution reaction by iron impurities in thin film nickel oxide electrodes. *J. Electrochem. Soc.* **134**, 377 (1987). [doi:10.1149/1.2100463](https://doi.org/10.1149/1.2100463)
7. J. Bao, X. Zhang, B. Fan, J. Zhang, M. Zhou, W. Yang, X. Hu, H. Wang, B. Pan, Y. Xie, Ultrathin spinel-structured nanosheets rich in oxygen deficiencies for enhanced electrocatalytic water oxidation. *Angew. Chem. Int. Ed.* **54**, 7399–7404 (2015). [doi:10.1002/anie.201502226](https://doi.org/10.1002/anie.201502226)
8. M. S. Burke, L. J. Enman, A. S. Batchellor, S. Zou, S. W. Boettcher, Oxygen evolution reaction electrocatalysis on transition metal oxides and (oxy)hydroxides: Activity trends and design principles. *Chem. Mater.* **27**, 7549–7558 (2015). [doi:10.1021/acs.chemmater.5b03148](https://doi.org/10.1021/acs.chemmater.5b03148)
9. N. Danilovic, R. Subbaraman, K.-C. Chang, S. H. Chang, Y. J. Kang, J. Snyder, A. P. Paulikas, D. Strmcnik, Y.-T. Kim, D. Myers, V. R. Stamenkovic, N. M. Markovic, Activity–stability trends for the oxygen evolution reaction on monometallic oxides in acidic environments. *J. Phys. Chem. Lett.* **5**, 2474–2478 (2014). [doi:10.1021/jz501061n](https://doi.org/10.1021/jz501061n)
10. M. Carmo, D. L. Fritz, J. Mergel, D. Stolten, A comprehensive review on PEM water electrolysis. *Int. J. Hydrogen Energy* **38**, 4901–4934 (2013). [doi:10.1016/j.ijhydene.2013.01.151](https://doi.org/10.1016/j.ijhydene.2013.01.151)
11. R. Tang, Y. Nie, J. K. Kawasaki, D.-Y. Kuo, G. Petretto, G. Hautier, G.-M. Rignanese, K. M. Shen, D. G. Schlom, J. Suntivich, Oxygen evolution reaction electrocatalysis on SrIrO₃ grown using molecular beam epitaxy. *J. Mater. Chem. A* **4**, 6831–6836 (2016). [doi:10.1039/C5TA09530A](https://doi.org/10.1039/C5TA09530A)
12. K. Nishio, H. Y. Hwang, Y. Hikita, Thermodynamic guiding principles in selective synthesis of strontium iridate Ruddlesden-Popper epitaxial films. *APL Mater.* **4**, 036102 (2016). [doi:10.1063/1.4943519](https://doi.org/10.1063/1.4943519)

13. Y. Lee, J. Suntivich, K. J. May, E. E. Perry, Y. Shao-Horn, Synthesis and activities of rutile IrO_2 and RuO_2 nanoparticles for oxygen evolution in acid and alkaline solutions. *J. Phys. Chem. Lett.* **3**, 399–404 (2012). [Medline](#) [doi:10.1021/jz2016507](#)
14. I. C. Man, H.-Y. Su, F. Calle-Vallejo, H. A. Hansen, J. I. Martínez, N. G. Inoglu, J. Kitchin, T. F. Jaramillo, J. K. Nørskov, J. Rossmeisl, Universality in oxygen evolution electrocatalysis on oxide surfaces. *ChemCatChem* **3**, 1159–1165 (2011). [doi:10.1002/cctc.201000397](#)
15. J. Rossmeisl, Z. W. Qu, H. Zhu, G. J. Kroes, J. K. Nørskov, Electrolysis of water on oxide surfaces. *J. Electroanal. Chem.* **607**, 83–89 (2007). [doi:10.1016/j.jelechem.2006.11.008](#)
16. H. W. Nesbitt, G. M. Bancroft, W. S. Fyfe, S. N. Karkhanis, A. Nishijima, S. Shin, Thermodynamic stability and kinetics of perovskite dissolution. *Nature* **289**, 358–362 (1981). [doi:10.1038/289358a0](#)
17. Z. Zhang, A low-temperature and low-cost method to produce high-quality epitaxial anatase TiO_2 thin films. *J. Mater. Res.* **20**, 292–294 (2005). [doi:10.1557/JMR.2005.0036](#)
18. Z. Xu, J. R. Kitchin, Tuning oxide activity through modification of the crystal and electronic structure: From strain to potential polymorphs. *Phys. Chem. Chem. Phys.* **17**, 28943–28949 (2015). [Medline](#) [doi:10.1039/C5CP04840K](#)
19. Y. K. Kim, A. Sumi, K. Takahashi, S. Yokoyama, S. Ito, T. Watanabe, K. Akiyama, S. Kaneko, K. Saito, H. Funakubo, Metalorganic chemical vapor deposition of epitaxial perovskite SrIrO_3 films on (100) SrTiO_3 substrates. *Jpn. J. Appl. Phys.* **45**, L36–L38 (2006). [doi:10.1143/JJAP.45.L36](#)
20. J. Matsuno, K. Ihara, S. Yamamura, H. Wadati, K. Ishii, V. V. Shankar, H. Y. Kee, H. Takagi, Engineering a spin-orbital magnetic insulator by tailoring superlattices. *Phys. Rev. Lett.* **114**, 247209 (2015). [Medline](#) [doi:10.1103/PhysRevLett.114.247209](#)
21. J. M. Kahk, C. G. Poll, F. E. Oropeza, J. M. Ablett, D. Céolin, J. P. Rueff, S. Agrestini, Y. Utsumi, K. D. Tsuei, Y. F. Liao, F. Borgatti, G. Panaccione, A. Regoutz, R. G. Egdel, B. J. Morgan, D. O. Scanlon, D. J. Payne, Understanding the electronic structure of IrO_2 using hard-x-ray photoelectron spectroscopy and density-functional theory. *Phys. Rev. Lett.* **112**, 117601 (2014). [Medline](#) [doi:10.1103/PhysRevLett.112.117601](#)
22. T. Reier, D. Teschner, T. Lunkenbein, A. Bergmann, S. Selve, R. Kraehnert, R. Schlögl, P. Strasser, Electrocatalytic oxygen evolution on iridium oxide: Uncovering catalyst-substrate interactions and active iridium oxide species. *J. Electrochem. Soc.* **161**, F876–F882 (2014). [doi:10.1149/2.0411409jes](#)
23. H. G. Sanchez Casalongue, M. L. Ng, S. Kaya, D. Friebe, H. Ogasawara, A. Nilsson, In situ observation of surface species on iridium oxide nanoparticles during the oxygen evolution reaction. *Angew. Chem. Int. Ed.* **53**, 7169–7172 (2014). [doi:10.1002/anie.201402311](#)
24. S. R. Bahn, K. W. Jacobsen, An object-oriented scripting interface to a legacy electronic structure code. *Comput. Sci. Eng.* **4**, 56–66 (2002). [doi:10.1109/5992.998641](#)
25. P. Giannozzi, S. Baroni, N. Bonini, M. Calandra, R. Car, C. Cavazzoni, D. Ceresoli, G. L. Chiarotti, M. Cococcioni, I. Dabo, A. Dal Corso, S. de Gironcoli, S. Fabris, G. Fratesi, R.

- Gebauer, U. Gerstmann, C. Gougoussis, A. Kokalj, M. Lazzeri, L. Martin-Samos, N. Marzari, F. Mauri, R. Mazzarello, S. Paolini, A. Pasquarello, L. Paulatto, C. Sbraccia, S. Scandolo, G. Sclauzero, A. P. Seitsonen, A. Smogunov, P. Umari, R. M. Wentzcovitch, QUANTUM ESPRESSO: A modular and open-source software project for quantum simulations of materials. *J. Phys. Condens. Matter* **21**, 395502 (2009). [Medline](#) [doi:10.1088/0953-8984/21/39/395502](https://doi.org/10.1088/0953-8984/21/39/395502)
26. B. Hammer, L. B. Hansen, J. K. Nørskov, Improved adsorption energetics within density-functional theory using revised Perdew-Burke-Ernzerhof functionals. *Phys. Rev. B* **59**, 7413–7421 (1999). [doi:10.1103/PhysRevB.59.7413](https://doi.org/10.1103/PhysRevB.59.7413)
 27. K. A. Stoerzinger, L. Qiao, M. D. Biegalski, Y. Shao-Horn, Orientation-dependent oxygen evolution activities of rutile IrO₂ and RuO₂. *J. Phys. Chem. Lett.* **5**, 1636–1641 (2014). [Medline](#) [doi:10.1021/jz500610u](https://doi.org/10.1021/jz500610u)
 28. B. Zhang, X. Zheng, O. Voznyy, R. Comin, M. Bajdich, M. García-Melchor, L. Han, J. Xu, M. Liu, L. Zheng, F. P. García de Arquer, C. T. Dinh, F. Fan, M. Yuan, E. Yassitepe, N. Chen, T. Regier, P. Liu, Y. Li, P. De Luna, A. Janmohamed, H. L. Xin, H. Yang, A. Vojvodic, E. H. Sargent, Homogeneously dispersed multimetal oxygen-evolving catalysts. *Science* **352**, 333–337 (2016). [Medline](#) [doi:10.1126/science.aaf1525](https://doi.org/10.1126/science.aaf1525)
 29. J. W. D. Ng, M. García-Melchor, M. Bajdich, P. Chakthranont, C. Kirk, A. Vojvodic, T. F. Jaramillo, Gold-supported cerium-doped NiO_x catalysts for water oxidation. *Nat. Energy* **1**, 16053 (2016). [doi:10.1038/nenergy.2016.53](https://doi.org/10.1038/nenergy.2016.53)
 30. M. Gong, Y. Li, H. Wang, Y. Liang, J. Z. Wu, J. Zhou, J. Wang, T. Regier, F. Wei, H. Dai, An advanced Ni–Fe layered double hydroxide electrocatalyst for water oxidation. *JACS* **135**, 8452–8455 (2013). [doi:10.1021/ja4027715](https://doi.org/10.1021/ja4027715)
 31. Z. Lu, W. Xu, W. Zhu, Q. Yang, X. Lei, J. Liu, Y. Li, X. Sun, X. Duan, Three-dimensional NiFe layered double hydroxide film for high-efficiency oxygen evolution reaction. *Chem. Commun. (Camb.)* **50**, 6479 (2014). [doi:10.1039/c4cc01625d](https://doi.org/10.1039/c4cc01625d)
 32. J. Y. C. Chen, L. Dang, H. Liang, W. Bi, J. B. Gerken, S. Jin, E. E. Alp, S. S. Stahl, Operando analysis of NiFe and Fe oxyhydroxide electrocatalysts for water oxidation: Detection of Fe⁴⁺ by Mössbauer spectroscopy. *JACS* **137**, 15090–15093 (2015). [doi:10.1021/jacs.5b10699](https://doi.org/10.1021/jacs.5b10699)
 33. X. Cui, P. Ren, D. Deng, J. Deng, X. Bao, Single layer graphene encapsulating non-precious metals as high-performance electrocatalysts for water oxidation. *Energy Environ. Sci.* **9**, 123–129 (2016).
 34. T. Audichon, T. W. Napporn, C. Canaff, C. Morais, C. Comminges, K. B. Kokoh, IrO₂ coated on RuO₂ as efficient and stable electroactive nanocatalysts for electrochemical water splitting. *J. Phys. Chem. C* **120**, 2562–2573 (2016). [doi:10.1021/acs.jpcc.5b11868](https://doi.org/10.1021/acs.jpcc.5b11868)
 35. E. Skúlason, V. Tripkovic, M. E. Björketun, S. Gudmundsdóttir, G. Karlberg, J. Rossmeisl, T. Bligaard, H. Jónsson, J. K. Nørskov, Modeling the electrochemical hydrogen oxidation and evolution reactions on the basis of density functional theory calculations. *J. Phys. Chem. C* **114**, 18182–18197 (2010). [doi:10.1021/jp1048887](https://doi.org/10.1021/jp1048887)
 36. A. C. Lausche, A. J. Medford, T. S. Khan, Y. Xu, T. Bligaard, F. Abild-Pedersen, J. K. Nørskov, F. Studt, On the effect of coverage-dependent adsorbate–adsorbate interactions

- for CO methanation on transition metal surfaces. *J. Catal.* **307**, 275–282 (2013). [doi:10.1016/j.jcat.2013.08.002](https://doi.org/10.1016/j.jcat.2013.08.002)
37. A. D. Doyle, J. H. Montoya, A. Vojvodic, Improving oxygen electrochemistry through nanoscopic confinement. *ChemCatChem* **7**, 738–742 (2015). [doi:10.1002/cctc.201402864](https://doi.org/10.1002/cctc.201402864)
38. X. Rong, J. Parolin, A. M. Kolpak, A fundamental relationship between reaction mechanism and stability in metal oxide catalysts for oxygen evolution. *ACS Catal.* **6**, 1153–1158 (2016). [doi:10.1021/acscatal.5b02432](https://doi.org/10.1021/acscatal.5b02432)
39. P. Vanysek, “Electrochemical series,” in *CRC Handbook of Chemistry and Physics*, D. R. Lide, Ed. (CRC Press, vol. 5, 1998), pp. 8-24.
40. Y. Liu, H. Masumoto, T. Goto, Structural, electrical and optical characterization of SrIrO₃ thin films prepared by laser-ablation. *Mater. Trans.* **46**, 100–104 (2005). [doi:10.2320/matertrans.46.100](https://doi.org/10.2320/matertrans.46.100)
41. L. Zhang, H.-Y. Wu, J. Zhou, F.-X. Wu, Y. B. Chen, S.-H. Yao, S.-T. Zhang, Y.-F. Chen, TEM study of SrIrO₃ thin films with various thicknesses grown on (001) SrTiO₃ substrates synthesized by pulsed laser deposition. *Appl. Surf. Sci.* **280**, 282–286 (2013). [doi:10.1016/j.apsusc.2013.04.150](https://doi.org/10.1016/j.apsusc.2013.04.150)
42. K. T. Jacob, T. H. Okabe, T. Uda, Y. Waseda, Phase relations in the system Sr–Ir–O and thermodynamic measurements on SrIrO₃, Sr₂IrO₄ and Sr₄IrO₆ using solid-state cells with buffer electrodes. *J. Alloys Compd.* **288**, 188–196 (1999). [doi:10.1016/S0925-8388\(99\)00089-4](https://doi.org/10.1016/S0925-8388(99)00089-4)
43. W. B. White, in *Corrosion of Glass, Ceramics and Ceramic Superconductors*, D. E. Clark, B. K. Zaitos, Eds. (Noyes Publications, 1992), pp. 2–28.
44. M. Kawasaki, K. Takahashi, T. Maeda, R. Tsuchiya, M. Shinohara, O. Ishiyama, T. Yonezawa, M. Yoshimoto, H. Koinuma, Atomic control of the SrTiO₃ crystal surface. *Science* **266**, 1540–1542 (1994). [Medline doi:10.1126/science.266.5190.1540](https://pubmed.ncbi.nlm.nih.gov/11265190/)
45. G. Koster, B. L. Kropman, G. J. H. M. Rijnders, D. H. A. Blank, H. Rogalla, Quasi-ideal strontium titanate crystal surfaces through formation of strontium hydroxide. *Appl. Phys. Lett.* **73**, 2920 (1998). [doi:10.1063/1.122630](https://doi.org/10.1063/1.122630)
46. J. G. Connell, B. J. Isaac, G. B. Ekanayake, D. R. Strachan, S. S. A. Seo, Preparation of atomically flat SrTiO₃ surfaces using a deionized-water leaching and thermal annealing procedure. *Appl. Phys. Lett.* **101**, 251607 (2012). [doi:10.1063/1.4773052](https://doi.org/10.1063/1.4773052)
47. D. W. Readey, in *Environmental Degradation of Advanced and Traditional Engineering Materials*, L. H. Hihara, R. P. I. Adler, R. M. Latanision, Eds. (CRC Press, 2013), pp. 511–526.
48. K. J. May, C. E. Carlton, K. A. Stoerzinger, M. Risch, J. Suntivich, Y.-L. Lee, A. Grimaud, Y. Shao-Horn, Influence of oxygen evolution during water oxidation on the surface of perovskite oxide catalysts. *J. Phys. Chem. Lett.* **3**, 3264–3270 (2012). [doi:10.1021/jz301414z](https://doi.org/10.1021/jz301414z)
49. M. Risch, A. Grimaud, K. J. May, K. A. Stoerzinger, T. J. Chen, A. N. Mansour, Y. Shao-Horn, Structural changes of cobalt-based perovskites upon water oxidation investigated by EXAFS. *J. Phys. Chem. C* **117**, 8628–8635 (2013). [doi:10.1021/jp3126768](https://doi.org/10.1021/jp3126768)

50. A. V. Naumkin, A. Kraut-Vass, S. W. Gaarenstroom, C. J. Powell, NIST Standard Reference Database 20, Version 4.1 (National Institute of Standards and Technology, 2012); <http://srdata.nist.gov/xps>.
51. ThermoFisher, Thermo Scientific XPS Advantage Data System; <http://xpssimplified.com>.
52. V. Young, T. Otagawa, XPS studies on strontium compounds. *Appl. Surf. Sci.* **20**, 228–248 (1985). [doi:10.1016/0378-5963\(85\)90083-2](https://doi.org/10.1016/0378-5963(85)90083-2)